Text Supplement for ScholarWorks@UA collection
Seismic moment tensors for six events in the Minto Flats fault zone, 2012–2016

Vipul Silwal

Version 1: April 4, 2018

Attribution: If you use these files, please cite *Tape et al.* (2018) and *Silwal* (2018).

Description of files

This collection is established as a supplement to a published manuscript (*Tape et al.*, 2018).

Seismic moment tensors were estimated using body waves and surface waves. The best solution (M_0) was obtained through a grid-search in the moment tensor space using the 'cut-and-paste' (CAP) approach, which allows for different frequencies and time shifts on different portions of seismograms (*Zhao and Helmberger*, 1994; *Zhu and Helmberger*, 1996; *Zhu and Ben-Zion*, 2013). The moment tensor approach was adapted and applied in *Silwal and Tape* (2016) and *Silwal et al.* (2018) for double couple moment tensors and in *Alvizuri and Tape* (2016) for full moment tensors.

A summary of files in the collection is listed in the following table:

file name	description
scholarworks.pdf	this file: summary of collection
waveform_fits_ALL.pdf	Figure A: waveform fits
beachballs_ALL.pdf	Figure B: beachball plots with piercing points
depth_tests_ALL.pdf	Figure C: depth grid search plots
nennuc_mech.txt	text file catalog of moment tensors
nennuc_weights.zip	zipped set of text files of input parameters for moment tensor inversions
nennuc_mt.pdf	moment tensor inversions with varying source duration

Within each set of figures (A, B, C), the 6 events are in chronological order by origin time.

Figure A: Waveform fits

Waveform fits for 6 moment tensor inversions. An example is included here as Figure A3. Black are observed waveforms; red are synthetic waveforms computed using a frequency-wavenumber method (*Zhu and Rivera*, 2002) that assumes a (1D) layered model. The waveforms are fit separately within five time windows: P wave vertical component (PV), P wave radial component (PR), Rayleigh wave vertical component (SurfV), Rayleigh wave horizontal component (SurfR), and Love wave transverse component (SurfT). At far left in each row is the station name, source-station distance in km, and station azimuth in degrees. Below each pair of waveforms are four numbers: the cross-correlation time shift between data and synthetics, the cross-correlation value, the percent of the misfit function represented by the waveform pair, and the amplitude ratio between waveforms, $\ln(A_{\mathrm{obs}}/A_{\mathrm{syn}})$, where A is the max value of the waveform within the time window.

The beachball represents the best solution M_0 (i.e., the global minimum of the misfit function). The beachball is plotted as a lower-hemisphere projection (standard seismological convention) of the moment tensor. The surrounding black dots denote the azimuthal location of the stations used, and the red crosses denote the lower hemisphere piercing points of the ray paths to the stations.

Here is a header for an example event in Figure A3: The four header lines are as follows:

1. `Event 20150912032512711 Model tactmod Depth 21`
   The event ID is derived from the origin time of 2015-09-12 03:25:12.711.
   The layered model used is `tactmod`, and the event depth is 21 km.

2. `FM 211 50 -16 Mw 3.80 γ 0 δ 0 rms 2.253e-01 VR 94.9 pol_wt 999.00`

   The orientation of the moment tensor solution M_0 is strike 211°, dip 50°, rake −16°. The estimated magnitude is M_w 3.8. The source type of M_0 is expressed in terms of lune longitude $\gamma = 0°$ and lune latitude $\delta = 0°$. Since we are searching only in double couple space, γ and δ are zero for all solutions (see (*Alvizuri et al.*, 2018)). The waveform difference between data and synthetics is $RMS = 2.253e-01$, and the variance reduction is $VR = 94.9\%$. These are based on a waveform difference measure that rewards using longer time windows and broader bandpass limits. This choice means that the VR cannot be directly compared with VR values reported in other studies. If polarities are use in the misfit function, then the factor `pol_wt` determines the balance between fitting waveforms and fitting polarities. A value of 999.0 means that polarities are not used.

3. `Filter periods (seconds): Body:0.50-2.50. Surf:20.00-50.00 duration: 12.00/6.00 s`
   The body waves were filtered 0.50–2.50 s, the surface waves were filtered 20.00–50.00 s. The source time function is a trapezoidal function whose duration is 12.00 s and whose rise time is half the duration. The duration is not an estimated source parameter but is set such that it gives the highest VR(see nennuc_mt.pdf for detailed analysis).

4. `# norm L1 # Pwin 6 Swin 200 # N 13 Np 0 Ns 38`
   An L1 norm was used for the misfit function (e.g., *Silwal and Tape*, 2016). The (reference) P-window is 6 s long and the surface wave window is 200 s long. Again, these parameters are meaningful only if the body or surface wave components are used for inversion. From a total of 13 stations (N), 0 P wave windows (Np), and 38 surface wave windows (Ns) were used. In this example, body waves are not used.

The numbers below each station are

1. source–station epicentral distance, km
2. station azimuth, in degrees
3. time shift between picked P onset and synthetic P onset.
4. sign of the observed first-motion polarity, which is either 1 (up or compression) or −1 (down or dilatation). The number in parentheses is the predicted amplitude, which ranges between $\pm\sqrt{2}$; numbers close to zero indicate that the station is near a nodal surface of the radiation pattern for the assumed mechanism.

The four numbers below each pair of waveforms are

1. the cross-correlation time shift $\Delta T = T_{obs} - T_{syn}$ required for matching the synthetics $s(t)$ with the data $u(t)$. A positive time-shift means that the synthetics arrive earlier than the data and that the assumed velocity model is faster than the actual earth structure.
2. the maximum cross-correlation percentage between $u(t)$ and $s(t - \Delta T)$
3. the percentage of the total misfit
4. the amplitude ratio $\ln(A_{obs}/A_{syn})$ in each time window

Figure B: Beachballs with piercing points

An example figure is shown in Figure B3.

The two header lines are as follows:

1. `Event 20150912032512711 Model 20150912032512711_tactmod_021`
   Same as the header line 1 for waveform fits plot.

2. `FM 211 50 -16 Mw 3.80` γ `0` δ `0 rms 2.253e-01 VR 94.9 pol_wt 999.00`
   Same as the header line 2 for waveform fits plot.

   The dot ($\cdot$) at the station name outside marks the source-station azimuth. The lower hemisphere piercing points are marked with a cross (x). The upper hemisphere piercing points are marked with a circle (o).

Figure C: Depth grid search plot

An example depth grid search plot is shown in Figure C3.

The plot shows the best-fitting depth grid search for 6 events. The depth increment for the grid search is 1 km. The red inverted triangle marks the Alaska Earthquake Center catalog depth, and the white inverted triangle marks the depth obtained from the moment tensor inversion. The blue tick marks on the x-axis mark the layer boundaries in the 1D model (`tactmod`) used in the moment tensor inversions. The plot shows the variance reduction (gray curve) with scale on the right. On the left is the variance reduction relative to the minimum variance reduction. The depth uncertainty is calculated based on the depth at which the variance reduction is 0.10 worse than at the best solution. Note that the earthquake magnitude is free to change for each depth, and it generally increases with increasing depth for the best-fitting solution (at a given depth), as we might expect.

Text file tables for moment tensor catalogs [`nennuc_mech.txt`]

Seismic moment tensor catalog for the 6 events. Details can be found within the header lines, which also refer to *Kanamori* (1977); *Aki and Richards* (1980); *Silver and Jordan* (1982); *Minson et al.* (2007); *Tape and Tape* (2012, 2013, 2015).

Input text files used in the moment tensor inversion [`nennuc_weights.zip`]

We provide a text file for each of the 6 events in this study. These files show which stations and which time windows were used (or not) in each moment tensor inversion. It also shows the first-motion polarity observations that were used.

References

Aki, K., and P. G. Richards (1980), *Quantitative Seismology, Theory and Methods*, W. H. Freeman, San Francisco, Calif., USA.

Alvizuri, C., and C. Tape (2016), Full moment tensors for small events ($M_{\rm w} < 3$) at Uturuncu volcano, Bolivia, *Geophys. J. Int.*, *206*, 1761–1783, doi:10.1093/gji/ggw247.

Alvizuri, C., V. Silwal, L. Krischer, and C. Tape (2018), Estimation of full moment tensors, including uncertainties, for nuclear explosions, volcanic events, and earthquakes, *J. Geophys. Res. Solid Earth* (in revision).

Kanamori, H. (1977), The energy release in great earthquakes, *J. Geophys. Res.*, *82*, 2981–2987.

Minson, S. E., D. S. Dreger, R. Bürgmann, H. Kanamori, and K. M. Larson (2007), Seismically and geodetically determined nondouble-couple source mechanisms from the 2000 Miyakejima volcanic earthquake swarm, *J. Geophys. Res.*, *112*, B10308, doi:10.1029/2006JB004847.

Silver, P. G., and T. H. Jordan (1982), Optimal estimation of scalar seismic moment, *Geophys. J. R. Astron. Soc.*, *70*, 755–787.

Silwal, V. (2018), Seismic moment tensors for six events in the Minto Flats fault zone, 2012–2016, ScholarWorks@UA: descriptor file, text file of catalog, figures with waveform fits, and input weight files.

Silwal, V., and C. Tape (2016), Seismic moment tensors and estimated uncertainties in southern Alaska, *J. Geophys. Res. Solid Earth*, *121*, 2772–2797, doi:10.1002/2015JB012588.

Silwal, V., C. Tape, and A. Lomax (2018), Crustal earthquakes in the Cook Inlet and Susitna region of southern Alaska, *Tectonophysics*(in review).

Tape, C., et al. (2018), Earthquake nucleation and fault slip complexity in the lower crust of central Alaska, *Nature Geoscience* (in review).

Tape, W., and C. Tape (2012), A geometric setting for moment tensors, *Geophys. J. Int.*, *190*, 476–498, doi:10.1111/j.1365-246X.2012.05491.x.

Tape, W., and C. Tape (2013), The classical model for moment tensors, *Geophys. J. Int.*, *195*, 1701–1720, doi:10.1093/gji/ggt302.

Tape, W., and C. Tape (2015), A uniform parameterization of moment tensors, *Geophys. J. Int.*, *202*, 2074–2081, doi:10.1093/gji/ggv262.

Zhao, L.-S., and D. V. Helmberger (1994), Source estimation from broadband regional seismograms, *Bull. Seismol. Soc. Am.*, *84*(1), 91–104.

Zhu, L., and Y. Ben-Zion (2013), Parameterization of general seismic potency and moment tensors for source inversion of seismic waveform data, *Geophys. J. Int.*, *194*, 839–843, doi:10.1093/gji/ggt137.

Zhu, L., and D. Helmberger (1996), Advancement in source estimation techniques using broadband regional seismograms, *Bull. Seismol. Soc. Am.*, *86*(5), 1634–1641.

Zhu, L., and L. A. Rivera (2002), A note on the dynamic and static displacements from a point source in multilayered media, *Geophys. J. Int.*, *148*, 619–627, doi:10.1046/j.1365-246X.2002.01610.x.

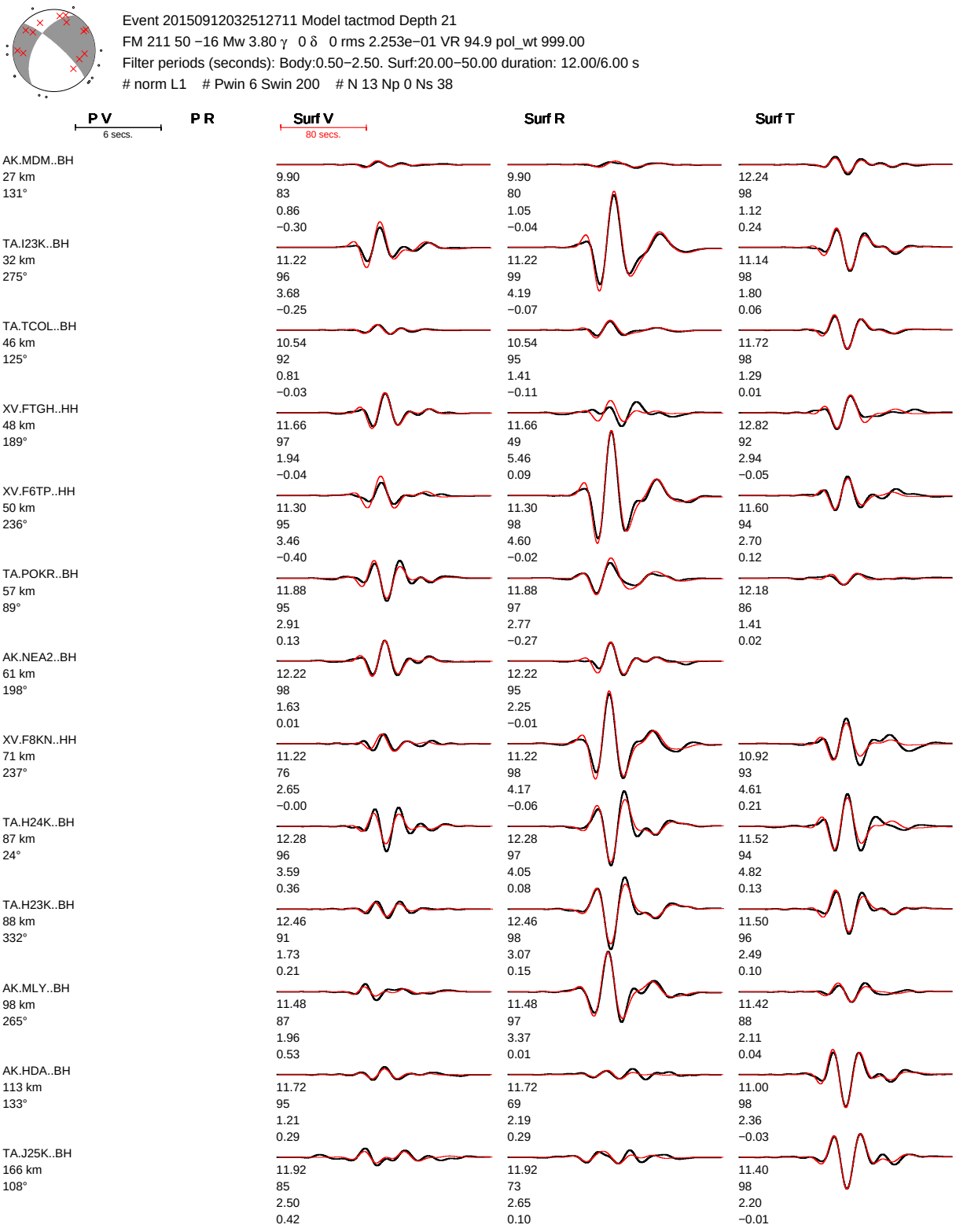

Figure A3: Example from p. 3 of the set of 6 pages in Figure A.

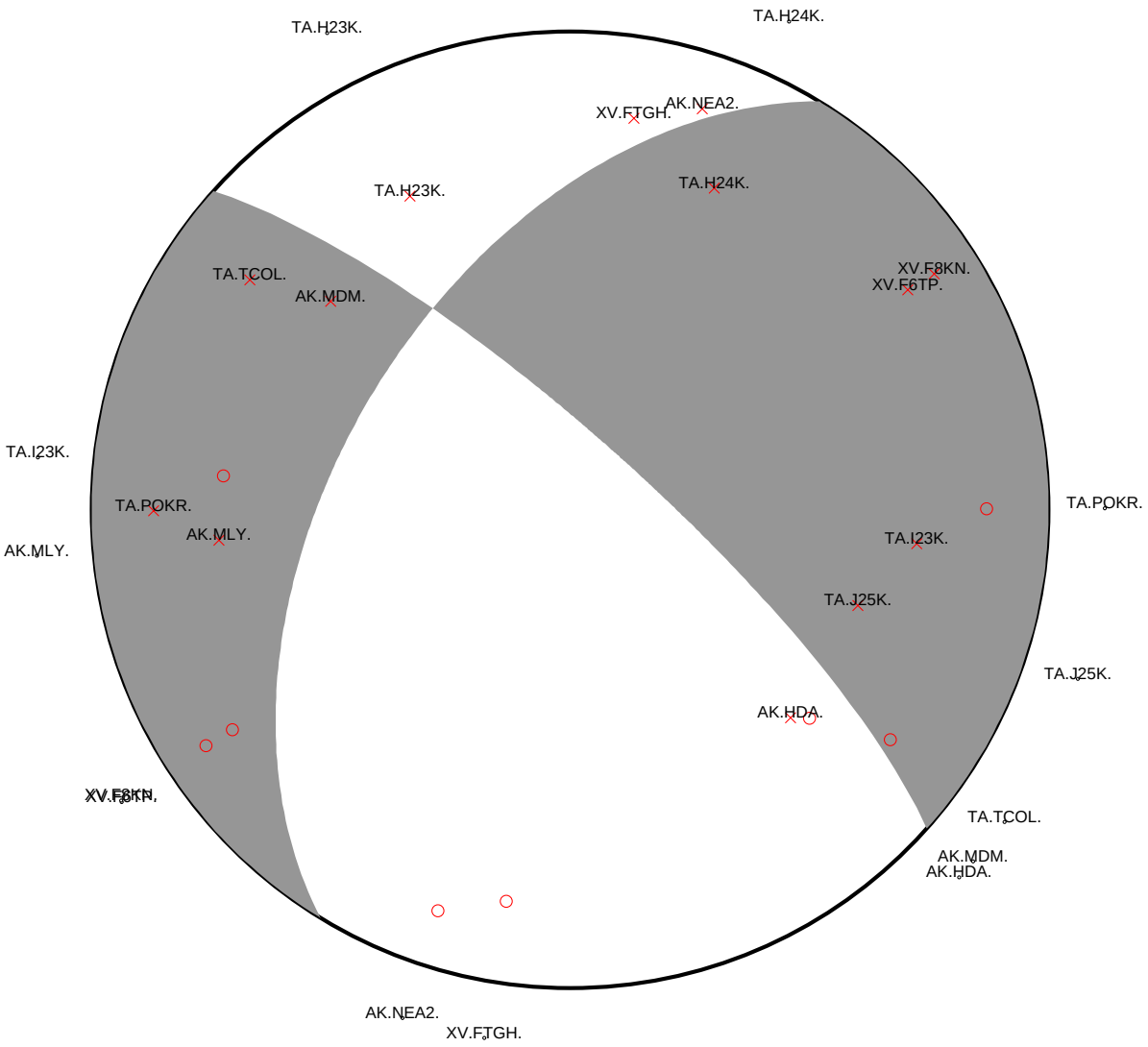

Figure B3: Example from p. 3 of the set of 6 pages in Figure B.

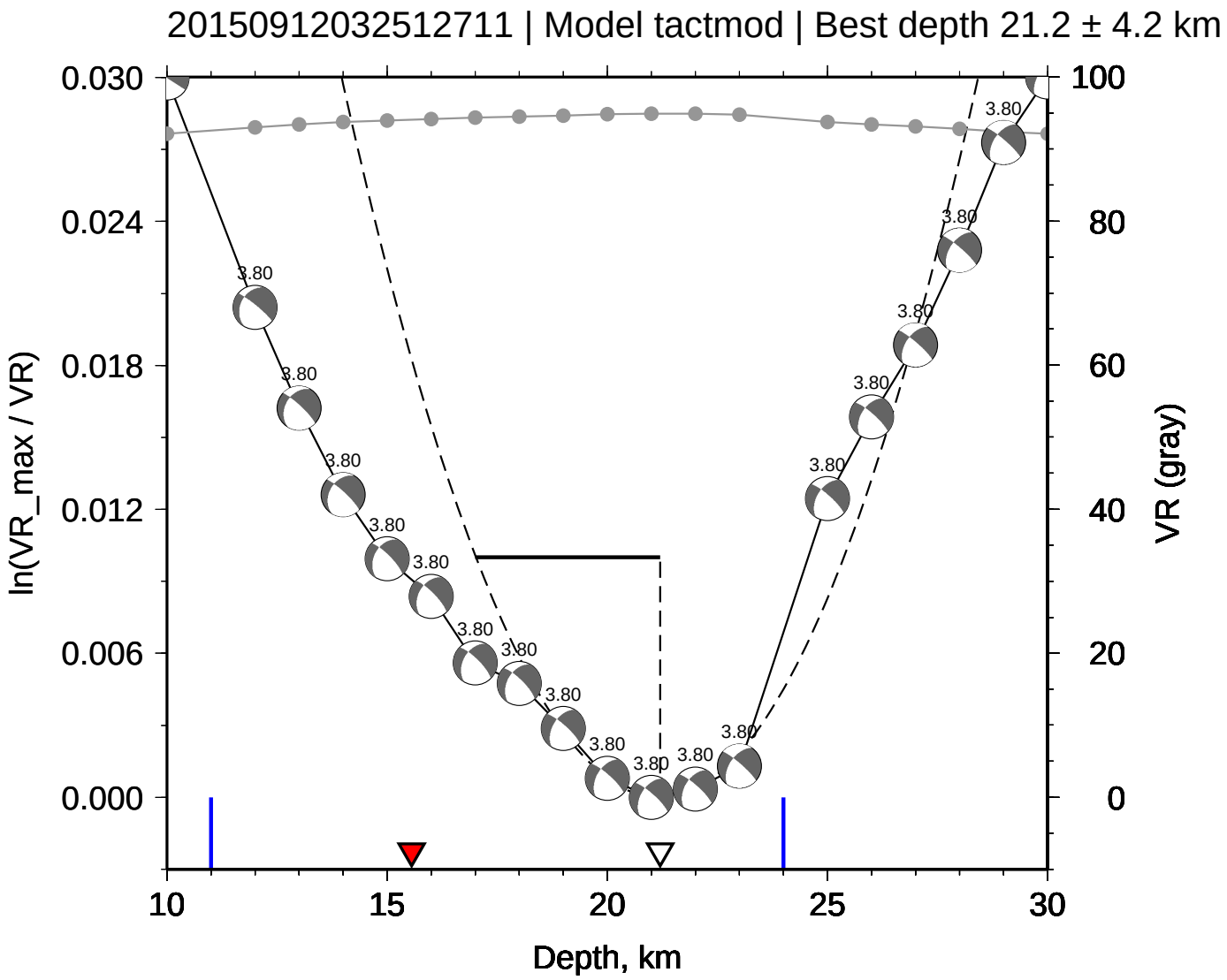

Figure C3: Example from p. 3 of the set of 6 pages in Figure C.